



Optics Letters

Aluminum nitride on insulator (AlNOI) platform for mid-infrared photonics

BOWEI DONG,^{1,3,7,8}  XIANSU LUO,² SHIYANG ZHU,³ MO LI,^{4,5} DIHAN HASAN,^{1,7} LI ZHANG,⁶ SOO JIN CHUA,⁶ JINGXUAN WEI,^{1,7}  YUHUA CHANG,^{1,7}  GUO-QIANG LO,² KAH WEE ANG,^{1,7}  DIM-LEE KWONG,³ AND CHENGKUO LEE^{1,7,8,*} 

¹Department of Electrical and Computer Engineering, National University of Singapore, Singapore 117576, Singapore

²Advanced Micro Foundry, Pte. Ltd., 11 Science Park Road, Singapore Science Park II, Singapore 117685, Singapore

³Institute of Microelectronics, Agency for Science, Technology and Research (A*STAR), Singapore 138634, Singapore

⁴Department of Electrical and Computer Engineering, University of Washington, Seattle, Washington 98195, USA

⁵Department of Physics, University of Washington, Seattle, Washington 98195, USA

⁶Low Energy Electronic Systems, Singapore-MIT Alliance for Research and Technology, Singapore 138602, Singapore

⁷Center for Intelligent Sensors and MEMS (CISM), National University of Singapore, Singapore 117576, Singapore

⁸Graduate School for Integrative Science and Engineering, National University of Singapore, Singapore 117456, Singapore

*Corresponding author: elelc@nus.edu.sg

Received 1 November 2018; accepted 20 November 2018; posted 28 November 2018 (Doc. ID 349563); published 20 December 2018

We report an aluminum nitride on insulator platform for mid-infrared (MIR) photonics applications beyond 3 μm . Propagation loss and bending loss are studied, while functional devices such as directional couplers, multimode interferometers, and add/drop filters are demonstrated with high performance. The complementary metal-oxide-semiconductor-compatible aluminum nitride offers advantages ranging from a large transparency window, high thermal and chemical resistance, to piezoelectric tunability and three-dimensional integration capability. This platform can have synergy with other photonics platforms to enable novel applications for sensing and thermal imaging in MIR. © 2018 Optical Society of America

<https://doi.org/10.1364/OL.44.000073>

Mid-infrared (MIR) beyond 3 μm is an important wavelength range in the electromagnetic wave spectrum [1]. It contains two atmospheric transmission windows (3–5 and 8–14 μm) which can open the possibility for remote sensing, thermal imaging, and infrared homing [2,3]. Meanwhile, it covers many vibrational molecular fingerprints, including C–H, N–H, C=C, C=O, O–H, etc. Hence, MIR is an ideal wavelength range for label-free spectroscopic sensing [4]. In particular, planar MIR devices (or MIR waveguide devices) can be fabricated using the matured complementary metal-oxide-semiconductor (CMOS) fabrication technology, making the mass manufacturing of low-cost and high-performance devices possible. To date, the sensing of methane [5], heavy water [6], exhaled breath [7], glucose [8], and volatile organic compounds (VOCs) [9] have been demonstrated in the MIR. However, one material platform cannot satisfy MIR applications in the whole spectrum, because each material platform is limited by its transparency window [10]. Therefore, several material platforms have been

investigated to develop a complete library for the MIR. These include silicon-on-insulator (SOI) [11], silicon-on-silicon nitride [12], silicon-on-sapphire [13], germanium-on-insulator [14], germanium-on-silicon (GOS) [15], germanium-on-silicon nitride [16], and silicon-germanium alloy (SiGe)-on-silicon (SGOS) [17].

Aluminum nitride (AlN) is a CMOS-compatible material commonly used for microelectromechanical systems (MEMS). By virtue of its large bandgap of 6.2 eV, the AlN transparency window spans from 0.2 to 13.6 μm [18]. Apart from high thermal and chemical resistance for harsh environment applications [19], AlN features a piezoelectric property for mechanical tuning [20] and a satisfactory Pockel's coefficient for nonlinear applications [21]. To date, various AlN photonics devices have been demonstrated such as waveguides [22], directional couplers (DCs) [23], grating couplers [24], ring resonators [25], and photonic crystals [26]. Applications ranging from second-harmonic generation [27], electro-optic modulation [28], acoustic wave modulated integrated resonators [29], and rotation detection are realized on the AlN photonics platform [30]. Nevertheless, none of these AlN photonics devices is operating in the MIR beyond 3 μm . Extending AlN photonics to a longer wavelength will bring substantial advantages to MIR applications enabled by the superior properties of AlN.

In this Letter, we demonstrate the AlN on insulator (AlNOI) platform for the broad MIR wavelength range from 3.66 to 3.90 μm for the first time, to the best of our knowledge. The fabrication is done in an 8 in CMOS manufacturing line, indicating the feasibility of mass production and integration with electronics. The platform is studied by both material characterization and device performance characterization. Propagation loss and bending loss are nearly constant across the measured wavelength range. Multimode interferometers (MMIs), DCs, and add/drop filters are investigated. These devices

exhibit high performance and low insertion loss. The potential applications and limitations of the presented AlNOI platform are discussed. This Letter demonstrates the feasibility of adopting an AlNOI platform for MIR beyond 3 μm and lays the foundations for novel applications in MIR integrated photonics.

The fabrication starts from an 8 in silicon (Si) wafer. The bottom cladding of 3.2 μm silicon dioxide (SiO_2) is deposited by plasma enhanced chemical vapor deposition (PECVD). The cladding is thinned to 3 μm by chemical-mechanical planarization to provide a smooth surface for AlN deposition. Subsequently, a device layer of 1.2 μm AlN is deposited by reaction DC magnetron sputtering, followed by SiO_2 hard mask deposition. Next, we pattern the SiO_2 hard mask using deep ultraviolet lithography, and transfer the patterns to the AlN device layer by deep reactive ion etching. 3 μm PECVD SiO_2 is then deposited as the upper cladding for passivation. Finally, a deep trench of more than 100 μm is formed for wafer dicing and fiber butt coupling.

Figure 1 shows the material characterization results of the AlNOI platform consisting of 1.2 μm AlN thin film on 3 μm SiO_2 on Si. The single X-ray diffraction (XRD) peak at 36.04° across the XRD spectrum in Fig. 1(a) reveals that the AlN thin film is highly c-axis (002) oriented [31]. The inset shows a full width at half-maximum (FWHM) of 0.16° , indicating the supreme piezoelectric property of the AlN thin film which comes close to the epitaxially grown AlN [32]. Figure 1(b) shows the transmission electron microscopy (TEM) image of the waveguide cross section. The facet is clear and smooth without significantly visible point defects or dislocations at material interfaces. A side wall slope of 77° is observed. The inset of Fig. 1(b) zooms in to the waveguide, showing the well-oriented texture of AlN in the c-axis normal to the wafer surface. The Raman spectrum is presented in Fig. 1(c).

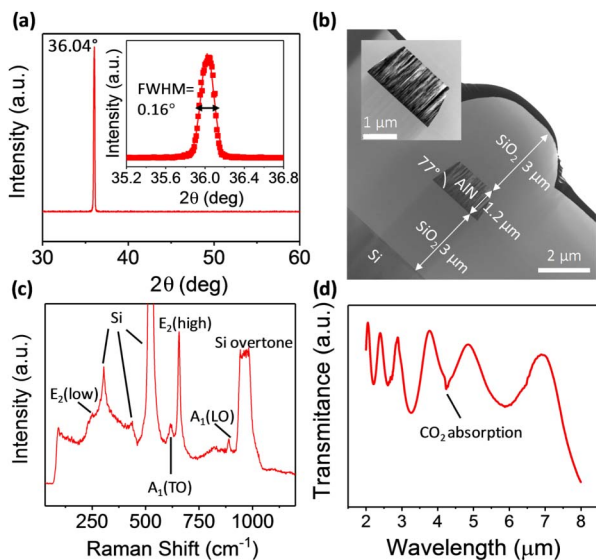


Fig. 1. Material characterization of the MIR AlNOI platform. (a) XRD pattern of the 1.2 μm AlN thin film on 3 μm SiO_2 on Si. Inset, zoom-in of the peak at 36.04° . (b) TEM image of the waveguide cross section. Inset, zoom-in of the waveguide. (c) Raman spectrum of the AlNOI platform. (d) FTIR spectrum of the AlNOI platform.

The characteristic phonon modes $E_2(\text{high})$, $A_1(\text{TO})$, $E_2(\text{low})$, and $A_1(\text{LO})$ are observed at around 659, 617, 249, and 888 cm^{-1} , respectively, which agrees well with the reported AlN Raman spectra [33,34]. Figure 1(d) shows the Fourier-transform infrared spectroscopy (FTIR) transmittance spectrum of the AlNOI platform in 2–8 μm measured in ambient. No obvious transmittance dip is observed, except a small dip at around 4.2 μm caused by carbon dioxide absorption originated from ambient air. It serves to verify that AlN is transparent in 2–8 μm . The oscillation pattern is attributed to the multilayer interference, while the general decreasing trend in transmittance is explained by SiO_2 absorption.

The waveguide devices with a width of 2.25 μm are characterized by the setup shown in Fig. 2(a). The light emits from the MIR laser, and passes through the half-wave plate and chopper before it is launched to a MIR fiber by a focal lens. The light is coupled to the device by end-facet butt coupling and received by an output fiber connected to the photodetector. The fiber device alignment is fine-tuned by two six-axis stages. The propagation loss is presented in Fig. 2(b). A cutback method is employed for loss extraction. The inset of Fig. 2(b) shows an exemplary curve measured at 3.8 μm where the slope of the linear fitting reveals the propagation loss. It can be seen in Fig. 2(b) that the waveguide propagation loss spectrum is relatively flat across the wavelength range with an average and standard deviation of -1.74 and 0.05 dB/mm, respectively. Figure 2(c) shows the bending loss of 90° waveguide bends. The bending loss scatters around -0.17 , -0.19 , and -0.54 dB/ 90° when the bending radius is $r = 25$, 50, and 75 μm , respectively. The positive relation between the bending loss and radius suggests that the propagation loss is dominant. Different waveguide tapers are also investigated to realize high fiber-to-chip coupling efficiency. All tapers with different tip widths are tapered adiabatically to 2.25 over 200 μm propagation length. The fiber-to-chip coupling

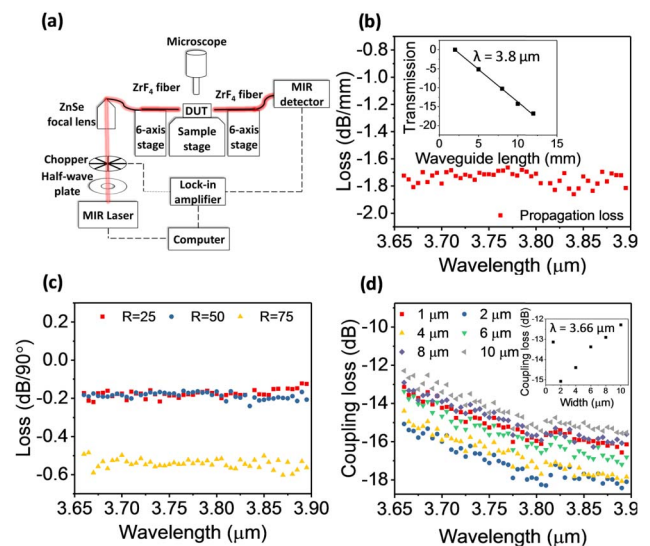


Fig. 2. (a) Optical testing setup. The dashed lines show an equipment connection, while the glowing red lines show the light path. (b) Propagation loss spectrum of waveguides. Inset, results measured by the cutback method at 3.8 μm . (c) Bending loss spectrum of waveguide bends. (d) Fiber-to-chip coupling loss of waveguide tapers with different tip widths. Inset, results at 3.66 μm .

efficiency of taper with different tip widths is shown in Fig. 2(d). In all tapers, the coupling loss increases as the wavelength rises due to a larger mode mismatch. At an individual wavelength, for instance, $3.66\ \mu\text{m}$ without loss of generality, the coupling loss is highest when the tip width is $2\ \mu\text{m}$. As the tip width decreases from 2 to $1\ \mu\text{m}$, the coupling loss drops from -15 to $-13\ \text{dB/facet}$, since the inverse taper with a smaller tip provides higher coupling efficiency. As the taper width rises from 2 to $10\ \mu\text{m}$, the coupling loss keeps decreasing and reaches around $-12\ \text{dB/facet}$, because forward tapers also enhance the coupling efficiency. Although this suggests that inverse tapers with smaller tips may achieve higher coupling efficiency, a tip width less than $1\ \mu\text{m}$ is difficult to fabricate due to the sloped sidewall. Therefore, in order to minimize coupling loss, wider forward taper should be designed with longer tapering length to ensure adiabatic tapering. The other solution is to use a grating coupler for higher coupling efficiency at the expense of a narrower bandwidth [35].

In order to explore the functionality of the AlNOI platform, we investigate the performance of DCs, MMIs, and add/drop filters built on this platform. The schematics and optical images of the devices are presented in Figs. 3(a)–3(c) with labeled design parameters. Figures 3(d)–3(f) show the scanning electron microscope (SEM) images of the fabricated devices before upper cladding deposition. The smooth sidewalls and clear gaps observed ensure the low insertion loss and high performance of these devices. The characterization of these functional building blocks is demonstrated in Fig. 4. Figure 4(a) presents the result of the 1×8 MMI splitter. Normalized outputs of -10.34 ± 0.42 , -9.75 ± 0.47 , -9.26 ± 0.68 , and $-9.44 \pm 0.70\ \text{dB}$ at 3.7 , 3.75 , 3.8 , and $3.85\ \mu\text{m}$, respectively, are measured from the eight output channels. Figure 4(b) shows the performance of the cascaded MMI splitter. The slopes extracted from linear fittings show insertion losses of -1.04 ± 0.48 , -0.71 ± 0.05 , -1.21 ± 0.13 , and $-0.98 \pm 0.25\ \text{dB}$ at 3.7 , 3.75 , 3.8 , and $3.85\ \mu\text{m}$, respectively. The 1×8 MMI splitter and the cascaded MMI splitter present figure of merit close to the theoretical value of -9 and $-3\ \text{dB}$, respectively, with low imbalance or variation. It is demonstrated that these devices have broadband operation capability.

A DC with gap $g = 0.4\ \mu\text{m}$ is also characterized. Figure 4(c) shows the self-normalized transmission in the transmitted port (T/I) and coupled port (X/I) of DCs with varying coupling lengths L_c at $3.7\ \mu\text{m}$. The data are fitted with a sine-squared

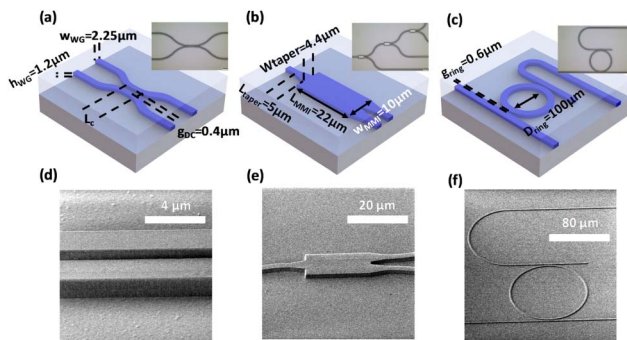


Fig. 3. Schematics, optical images, and SEM images of fabricated devices before upper cladding deposition. The designed parameters are labeled in schematics. (a) and (d) DC. (b) and (e) MMI. (c) and (f) Add-drop filter.

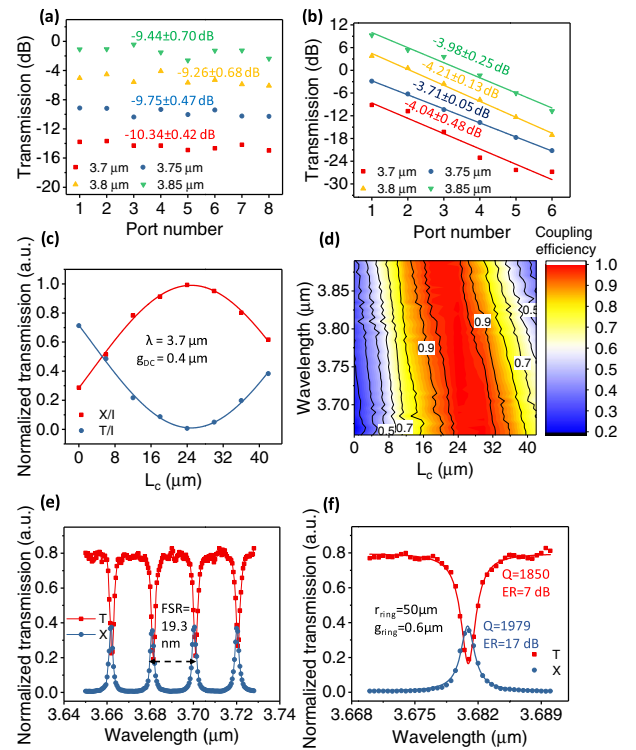


Fig. 4. Device characterization. (a) 1-to-8 MMI splitter. (b) Cascaded MMI splitter. (c) DC at $3.7\ \mu\text{m}$. (d) Coupling efficiency contour map for DCs. (e) Add-drop filter with $r = 50\ \mu\text{m}$. (f) Zoom-in of (e) to $3.68\ \mu\text{m}$.

function according to the coupled mode theory. An adj-R square of 0.999 is obtained, signifying good optical performance of the DC. We plot the contour map of coupling efficiency against the wavelength and L_c in Fig. 4(d). At the wavelength range of 3.66 – $3.90\ \mu\text{m}$, different coupling efficiencies could be achieved in DCs with suitable L_c . This contour map serves as a design guideline for DC in 3.66 – $3.90\ \mu\text{m}$ built on the presented AlNOI platform.

Add-drop filters are also demonstrated. In an add-drop filter with a ring radius of $50\ \mu\text{m}$ and gaps of $0.6\ \mu\text{m}$ at both the through port and drop port, a free spectral range of $19.3\ \text{nm}$ is obtained as shown in Fig. 4(e). The peak at $3.682\ \mu\text{m}$ is zoomed in with its result presented in Fig. 4(f) for further analysis. The solid lines showing the Lorentzian fit of the data demonstrate Q factor of 1850 and 1979 at the through port and drop port, respectively, while extinction ratios (ERs) of ~ 7 and $\sim 17\ \text{dB}$ are achieved. Meanwhile, an insertion loss of around $-1\ \text{dB}$ is observed in Fig. 4(f). These data show the high quality of the AlN add-drop filter in MIR which could enable high-precision MIR sensing and wavelength-division multiplexing in MIR.

The AlNOI platform working in the MIR beyond $3\ \mu\text{m}$ can bring many benefits. First, its prominent thermal and chemical resistance allow the platform to work in a harsh environment. We are developing other functional blocks, including nanocavities, slow light photonic crystal waveguides, and sub-wavelength structures to provide a full device library that complements the SOI counterpart [36–38]. Secondly, wafer-scale high-quality AlN thin film with c-axis orientation can be

deposited by reaction DC magnetron sputtering at a low temperature. This can potentially enable vertically stacked multiplayer photonics for three-dimensional integration. We have already manufactured AlN photonics integrated vertically on a SOI photonics platform which will be reported in the near future. Thirdly, by leveraging the AlN piezoelectricity, it is promising to realize MEMS actuators integrated with photonics in a single device layer. This could open the possibility for novel applications in MIR. Fourthly, as a high-speed SOI MIR modulator is limited by the abrupt increase in absorption due to free-carrier dispersion, an AlNOI platform can serve as an alternative for an MIR modulator by leveraging its high Pockel's coefficient. Nevertheless, our current result still shows high propagation loss in the AlNOI platform. It may limit current technology in applications such as a long-distance transmission line and an ultrahigh Q resonator that requires a low loss platform [39]. This suggests that the AlNOI platform cannot be a "solution-for-all" at present. It can be used in synergy with the SOI platform when SOI is used for long-distance transmission, and AlNOI for short-distance modulation. We are investigating theoretically and experimentally the solutions to lower the propagation loss in the AlNOI platform. Possible approaches include low-temperature annealing to further enhance the quality of the AlN thin film, replacing PECVD SiO₂ by TEOS SiO₂ or thermal SiO₂ for better cladding quality, and optimizing the etching process to achieve better sidewall smoothness and smaller slope. Furthermore, to fully utilize the AlN wide transparency window, a suspended membrane platform can be developed to prevent SiO₂ absorption loss [40].

In conclusion, we report, to the best of our knowledge, the first AlNOI platform for MIR applications beyond 3 μm . Approximately constant propagation loss and bending loss are measured in the wavelength range of 3.66–3.90 μm . Functional devices, including DCs, MMIs, and add/drop filters are demonstrated with high performance. Prominent imbalance of 0.42 dB and insertion loss of −0.71 dB are achieved in 1 × 8 MMI splitter and cascaded MMI, respectively. A Q factor of around 2000 with $ER = 17$ dB is demonstrated in an add/drop filter. AlN CMOS compatibility guarantees its bright future for low-cost and mass production. Its large bandgap makes it a potential candidate for broadband operation, while its thermal and chemical resistance allows it to work in harsh environments. The piezoelectric property and the low-temperature growth capability create the potential for synergy between the reported AlNOI photonics platform and other material platforms. This further enables three-dimensional integration for MEMS-based photonics and the realization of novel applications in MIR sensing and thermal imaging.

Funding. National Research Foundation Singapore (NRF) (NRF-CRP15-2015-02); National Natural Science Foundation of China (NSFC) (61474078).

REFERENCES

1. S. D. Jackson, *Nat. Photonics* **6**, 423 (2012).
2. Y. Zou, S. Chakravarty, C.-J. Chung, X. Xu, and R. T. Chen, *Photonics Res.* **6**, 254 (2018).
3. H. Lin, Z. Luo, T. Gu, L. C. Kimerling, K. Wada, A. Agarwal, and J. Hu, *Nanophotonics* **7**, 393 (2017).
4. T. Hu, B. Dong, X. Luo, T.-Y. Low, J. Song, C. Lee, and G. Lo, *Photonics Res.* **5**, 417 (2017).
5. L. Tombez, E. J. Zhang, J. S. Orcutt, S. Kamlapurkar, and W. M. J. Green, *Optica* **4**, 1322 (2017).
6. N. Singh, A. Casas-Bedoya, D. D. Hudson, A. Read, E. Mägi, and B. J. Eggleton, *Opt. Lett.* **41**, 5776 (2016).
7. B. Mizaikoff, *Chem. Soc. Rev.* **42**, 8683 (2013).
8. P. T. Lin, H. G. Lin, Z. Han, T. Jin, R. Millender, L. C. Kimerling, and A. Agarwal, *Adv. Opt. Mater.* **4**, 1755 (2016).
9. Y. Chen, H. Lin, J. Hu, and M. Li, *ACS Nano* **8**, 6955 (2014).
10. R. Soref, *Nat. Photonics* **4**, 495 (2010).
11. G. Z. Mashanovich, M. M. Milošević, M. Nedeljkovic, N. Owens, B. Xiong, E. J. Teo, and Y. Hu, *Opt. Express* **19**, 7112 (2011).
12. P. T. Lin, V. Singh, H. Y. G. Lin, T. Tiwald, L. C. Kimerling, and A. M. Agarwal, *Adv. Opt. Mater.* **1**, 732 (2013).
13. T. Baehr-jones, A. Spott, R. Ilic, A. Spott, B. Penkov, W. Asher, and M. Hochberg, *Opt. Express* **18**, 12127 (2010).
14. J. Kang, M. Takenaka, and S. Takagi, *Opt. Express* **24**, 11855 (2016).
15. D. A. Kozak, T. H. Stievater, R. Mahon, and W. S. Rabinovich, *J. Sel. Top. Quantum Electron.* **24**, 1 (2018).
16. W. Li, P. Anantha, S. Bao, K. H. Lee, X. Guo, T. Hu, L. Zhang, H. Wang, R. Soref, and C. S. Tan, *Appl. Phys. Lett.* **109**, 241101 (2016).
17. J. M. Ramirez, Q. Liu, V. Vakarín, J. Frigerio, A. Ballabio, X. Le Roux, D. Bouville, L. Vivien, G. Isella, and D. Marris-Morini, *Opt. Express* **26**, 870 (2018).
18. W. H. P. Pernice, C. Xiong, and H. X. Tang, *Opt. Express* **20**, 12261 (2012).
19. M. Gillinger, M. Schneider, A. Bittner, P. Nicolay, and U. Schmid, *J. Appl. Phys.* **117**, 065303 (2015).
20. A. Sanz-Hervás, M. Clement, E. Iborra, L. Vergara, J. Olivares, and J. Sangrador, *Appl. Phys. Lett.* **88**, 161915 (2006).
21. M. C. Larciprete, A. Bosco, A. Belardini, R. Li Voti, G. Leahu, C. Sibilia, E. Fazio, R. Ostuni, M. Bertolotti, A. Passaseo, B. Poti, and Z. Del Prete, *J. Appl. Phys.* **100**, 023507 (2006).
22. P. T. Lin, H. Jung, L. C. Kimerling, A. Agarwal, and H. X. Tang, *Laser Photonics Rev.* **8**, L23 (2014).
23. M. Stegmaier and W. H. P. Pernice, *Opt. Express* **21**, 7304 (2013).
24. S. Ghosh, C. R. Doerr, and G. Piazza, *Appl. Opt.* **51**, 3763 (2012).
25. H. Jung, M. Poot, and H. X. Tang, *Opt. Express* **23**, 30634 (2015).
26. W. H. P. Pernice, C. Xiong, C. Schuck, H. X. Tang, W. H. P. Pernice, C. Xiong, C. Schuck, and H. X. Tang, *Appl. Phys. Lett.* **100**, 091105 (2012).
27. X. Guo, C.-L. Zou, and H. X. Tang, *Optica* **3**, 1126 (2016).
28. S. Zhu and G.-Q. Lo, *Opt. Express* **24**, 12501 (2016).
29. S. A. Tadesse and M. Li, *Nat. Commun.* **5**, 5402 (2014).
30. M. Mahmoud, A. Mahmoud, L. Cai, M. Khan, T. Mukherjee, J. Bain, and G. Piazza, *Opt. Express* **26**, 25060 (2018).
31. N. Matsunami, H. Kakiuchida, M. Sataka, and S. Okayasu, *Adv. Mater. Phys. Chem.* **3**, 101 (2013).
32. R. S. Naik, J. J. Lutsky, R. Reif, C. G. Sodini, A. Becker, L. Fetter, H. Huggins, R. Miller, J. Pastalan, G. Rittenhouse, and Y. H. Wong, *IEEE Trans. Ultrason. Ferroelectr. Freq. Control* **47**, 292 (2000).
33. X. H. Ji, Q. Y. Zhang, Z. Y. Ling, and S. P. Lau, *Appl. Phys. Lett.* **95**, 233105 (2009).
34. S. Zuo, H. Zhang, J. Wang, and W. Wang, *Powder Diffr.* **29**, 3 (2014).
35. J. Kang, Z. Cheng, W. Zhou, T.-H. Xiao, K.-L. Gopalakrishna, M. Takenaka, H. K. Tsang, and K. Goda, *Opt. Lett.* **42**, 2094 (2017).
36. J. Wei, F. Sun, B. Dong, Y. Ma, H. Tian, and C. Lee, *Opt. Lett.* **43**, 5407 (2018).
37. Y. Ma, B. Dong, B. Li, K.-W. Ang, and C. Lee, *Opt. Lett.* **43**, 5504 (2018).
38. B. Dong, T. Hu, X. Luo, Y. Chang, X. Guo, H. Wang, D.-L. Kwong, G.-Q. Lo, and C. Lee, *Nanomaterial* **8**, 893 (2018).
39. T.-H. Xiao, Z. Zhao, W. Zhou, C.-C. Yao, S. Y. Set, M. Takenaka, H. K. Tsang, Z. Cheng, and K. Goda, *Opt. Lett.* **43**, 2885 (2018).
40. Z. Cheng, X. Chen, C. Y. Wong, K. Xu, and H. K. Tsang, *IEEE Photonics J.* **4**, 1510 (2012).